
Interpretability and Generalization Bounds for Learning Spatial Physics

Alejandro Francisco Queiruga*
 Google
 alejandro.queiruga@gmail.com

Theo Gutman-Solo
 Google
 gutmansolo@google.com

Shuai Jiang
 Sandia National Lab
 sjiang@sandia.gov

Abstract

While there are many applications of machine learning (ML) to scientific problems that *look* promising, the eye test can be misleading compared to quantitative measures. Using numerical analysis techniques, we rigorously quantify the accuracy, convergence rates, and generalization bounds of certain ML models applied to linear differential equations (DEs) for parameter discovery or solution finding. Beyond the quantity and discretization of data, we identify that the function space of the data is critical to the generalization of the model. A similar lack of generalization is empirically demonstrated for commonly used models, including physics-specific techniques. Counterintuitively, we find that different classes of models can exhibit opposing generalization behaviors. Based on our theoretical analysis, we also introduce a new mechanistic interpretability lens on scientific models whereby Green’s function representations can be extracted from the weights of black-box models. Our results inform a new cross-validation technique for measuring generalization in physical systems, which can serve as a benchmark.

1 Introduction

The development of robust and rigorous a priori estimates for numerical methods is a major victory of the past half-century. These estimates give geometric flexibility and convergence guarantees, laying the groundwork for complex physics simulations across a wide range of applications. The basis of the theory begins with the humble 1D Poisson equation, studied by virtually all numerical analysts and serving as the bedrock for computational physics and engineering.

The canonical Poisson equation on the unit interval with homogeneous Dirichlet boundary conditions is given by

$$-k \frac{d^2 u}{dx^2} = f(x), \quad u(0) = u(1) = 0. \quad (1)$$

where $u(x)$, $f(x)$, k are the solution, forcing function, and (constant) material coefficient, respectively. The solution to Eq. (1) can be obtained using the Green’s function which maps a function $f(x)$ to the solution $u(x)$ as follows:

$$u(x) = \int_0^1 f(s)G(s, x) ds + (u_1 - u_0)x + u_0 \quad (2)$$

*Affiliation at time of work: Google.

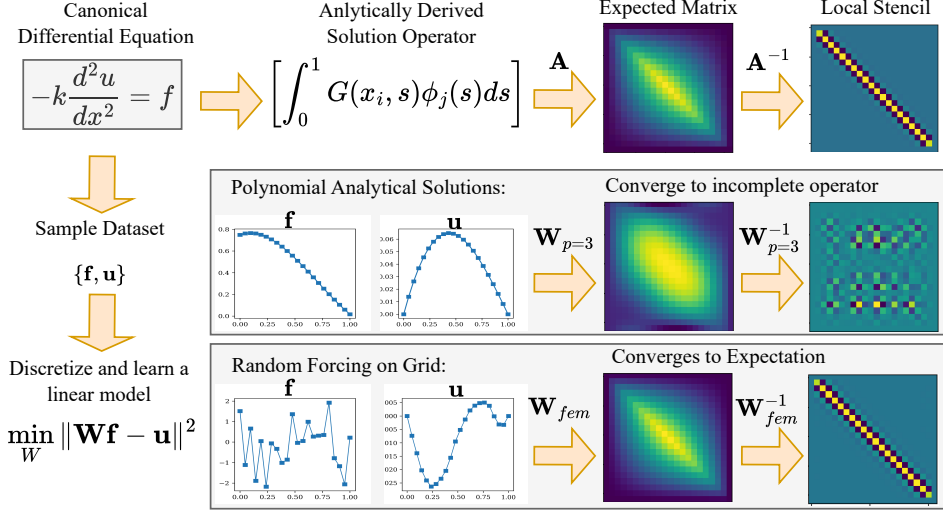


Figure 1: Expectations when learning a black box linear model, $\mathbf{u} = \mathbf{W}\mathbf{f}$. Despite some visual similarity to the Green’s function operator (top), naive approaches are not guaranteed to converge to the true operator. The issue lies in the sampling procedure of the training data. The naive approach of using polynomial analytical solutions (illustrated as cubic polynomials) can achieve machine precision MSE loss, but even with infinitely many examples, will not converge to the general solution (center). Altering the construction of the training data, i.e. by using random piecewise linear functions (bottom) can recover the true operator. This allows for the extraction of a familiar discrete differential equation operator (right).

where

$$G(s, x) = \begin{cases} (1-s)x & \text{if } x < s \\ (1-x)s & \text{if } x \geq s \end{cases} \quad (3)$$

In the ML context, the governing DE is typically unknown, and we are given discrete evaluations of forcing functions $f(x_i)$ and solutions $u(x_i)$ with $x_i \in (0, 1)$ corresponding to a sensor grid or pixels from a camera. We then seek to train a model approximating the solution operator that can compute an unknown u given an unseen f . While the DE is continuous, the act of measurement discretizes all objects. For simplicity, we only consider uniformly spaced points $x_i = i\Delta x$ for $i = 0, \dots, N_{\text{grid}}$.

The simplest black-box model is a linear operator given by

$$\mathbf{u} = \mathbf{W}\mathbf{f} \quad (4)$$

where $\mathbf{W} \in \mathbb{R}^{N_{\text{grid}} \times N_{\text{grid}}}$ and is trained via the usual gradient descent on mean squared error (MSE) loss, $\mathcal{L} = \sum \|\mathbf{u} - \mathbf{W}\mathbf{f}\|_2^2$. A natural question is what matrix this model learns; see Fig. 1. First, we constructed a dataset using analytical solutions with cubic forcing functions, and achieved low train and test error on that space. The learned matrix (second row) qualitatively resembles the analytically derived matrix from Green’s function (first row), but is quite far from the “truth” when we look at the inverse $\mathbf{W}_{p=3}^{-1}$. In general, the model will appear uninterpretable and fail to generalize to out-of-distribution (OOD) datasets. However, with careful construction of the dataset (bottom of Fig 1), we can recover both a full Green’s function discretization, \mathbf{A} and a discretization of the differential operator, $\mathbf{L} = \mathbf{A}^{-1}$.

To formalize, we define generalizability as achieving a low error when sampling from a different distribution than the training data. After minimizing $\mathcal{L}(W, \{u, f\} \sim \mathcal{F}_{\text{train}})$, we then desire that the model satisfy:

$$\mathcal{L}(W, \{u, f\} \sim \mathcal{F}_{\text{test}}) \lesssim \mathcal{L}(W, \{u, f\} \sim \mathcal{F}_{\text{train}}) \quad (5)$$

when $\mathcal{F}_{\text{test}} \neq \mathcal{F}_{\text{train}}$. The symbol \lesssim denotes a small “wobble room” tolerance heuristic. We empirically observe that the OOD error can be orders of magnitude larger than the observed training error, $\mathcal{L}_{\text{test}} \gg 10^8 \times \mathcal{L}_{\text{train}}$, which makes the OOD transition apparent.

We also design a new cross-validation procedure that trains a given ML model with a dataset on a subspace, and then evaluates the error on datasets generated on different *subspaces*. The datasets are

varied not only by the grid spacing Δx , but also by the function class $f \sim \mathcal{F}(\text{type}, p)$. We consider five different approaches and make present following contributions:

1. *Underparameterized models with an inductive bias of known physical equations* — We demonstrate both empirically and theoretically that the estimated w parameter converges to the true parameter k at a rate dependent upon the grid spacing Δx , finite difference order q , and which *increases* with the order of training function basis p .
2. *Exact parametrization for linear problems* — We derive a true solution \mathbf{A} , and theoretically and empirically demonstrate that the learned weights only converge to a subspace of the operator based on the basis of the training data. The grid size Δx does not change the error, but changes the scaling of learned parameters.
3. *Overparameterized neural models* — We empirically demonstrate that deep models *are not guaranteed to generalize* outside of the training data. Subspace generalization is also not guaranteed. It is possible to extract Green’s function operators from black-box models.
4. *Methods designed for DE learning* — We observe that the DeepONet and Fourier Neural Operator also do not always generalize, similarly to black-box models.
5. *Physics informed losses* — We demonstrate that PINNs and Physics Informed DeepONets, which incorporate prior DE knowledge, exhibit similar failure modes.

Surprisingly, we find that the data requirements and generalization behavior for each model class can vary dramatically, and in some cases, are even contrary to one another.

2 Background

Applications of ML in science span across “white-box” to “black-box”. White-box methods, such as SINDy and symbolic regression, allow for the obtainment of closed-form, analytical formulas (Rudy et al., 2017; Udrescu & Tegmark, 2020). Black-box methods such as Neural Operators or DeepONets generally use NNs to learn dynamics (Raissi et al., 2019; Lu et al., 2019), exchanging interpretability for flexibility. Between these two approaches, techniques have been developed that respect physical constraints such as conservation laws (Hansen et al., 2023; Patel et al., 2022; Trask et al., 2022). However, the adoption of these methods in high-consequence scenarios is lacking due to not understanding the exact failure modes.

To this end, recent studies have demonstrated that Neural ODEs and residual connections can overfit to time series data and may not learn true continuous models (Queiruga et al., 2020; Ott et al., 2021; Sander et al., 2022), whereas higher order time discretization can elicit generalization (Zhu et al., 2022; Krishnapriyan et al., 2023). For spatiotemporal models, Krishnapriyan et al. (2021) demonstrated that PINNs will fail without controlled training strategies, whereas Sakarvadia et al. (2025) showed that PINOs fail to generalize across spatial resolutions. The usage of Green’s functions in machine learning has been examined and used to prove data requirements for elliptic equations (Gin et al., 2021; Boullé et al., 2022, 2023). Direct inspection of weight matrices is an active area of research in mechanistic interpretability, where known algorithms can be found in the weights of ML models (Nanda et al., 2023). Interpretations of SciML mechanisms include drawing analogies between transformers and quadrature, nonlocal operators, or kernel functions (Cao, 2021; Nguyen et al., 2022; Yu et al., 2024).

3 Theoretical Results

3.1 Dataset construction

To explore how the functional source of training data impacts the model, we construct different datasets by sampling from different function spaces. Let $\mathcal{F}(\text{type}, p)$ denote a function space of a type (e.g., polynomial, FEM, cosine, sine, etc.) with p terms. Given the function class, the dataset is constructed by sampling functions evaluated on a grid with points $x_i \in i\Delta x$ with $\Delta x = 1/N_{\text{grid}}$ (e.g. the spacing the sensor grid). Entries in the dataset are $\{x_i, f(x_i), u(x_i)\}$ from functions sampled from $f \sim \mathcal{F}(\text{type}, p)$. In experiments, we consider function types of polynomial, sine $\sin(k\pi x)$, cosine $\cos(k\pi x)$, and piecewise linear.

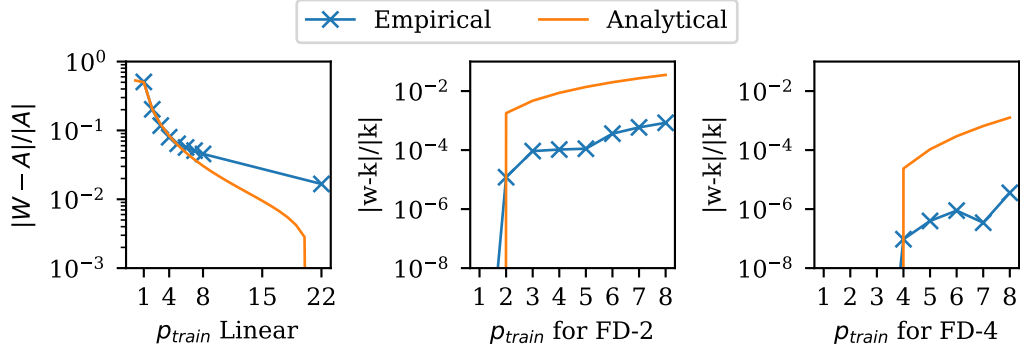


Figure 2: Comparison of numerical experiments to analytically derived ML parameters from Theorems 3.1 and 3.2 trained on polynomial spaces with $N_{grid} = 22$. (Left) The observed error for the linear matrix matches predictions for lower order p . (Middle and right) For the finite difference model, the analytical assumptions overestimate the error, but the trend matches with observations.

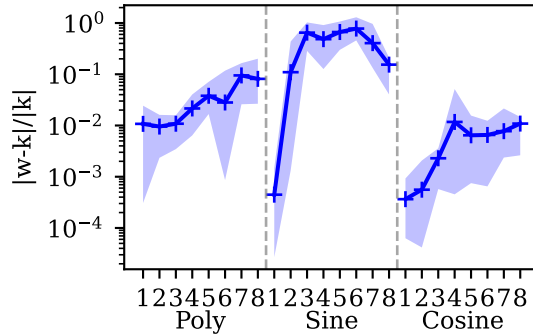


Figure 3: Learning a parameter using a PINN inverse problem. Line is the mean of five runs, and the shaded region covers the min-max spread.

3.2 Parameter learning with a discretized DE

Consider the case where the form of the DE is known, through either prior knowledge or a system identification method, but its physical parameters are unknown. We fit the discretized Poisson equation for a parameter w (whose true value is k from Eq. 1) such that $-w \frac{d^2 u(x_i)}{dx^2} \approx f(x_i)$ over the data. The DE is approximated using a standard finite difference stencil, such as the three-point stencil (FD-2),

$$\frac{d^2 u}{dx^2} = \frac{u_{i-1} - 2u_i + u_{i+1}}{\Delta x^2} + \mathcal{O}(\Delta x^2). \quad (6)$$

We can estimate w given the data $\{u, f\}$ by analytically minimizing the MSE loss over N examples

$$\frac{1}{N} \sum_{n=0}^N \sum_{i=1}^{N_{grid}-1} \left(\frac{w}{\Delta x^2} \left(u_{i-1}^{(n)} - 2u_i^{(n)} + u_{i+1}^{(n)} \right) + f_i^{(n)} \right)^2 \quad (7)$$

where superscript (n) indexes training examples. The following theorem shows that the relative error $e = |w - k|/|k|$ can be bounded for data sampled from polynomials:

Theorem 3.1. *Learning the parameter k using a finite difference stencil of order q given polynomial training data of degree p on a grid of spacing Δx results in $w = k$ when $p < q$, and an error*

$$\frac{|w - k|}{|k|} = \mu_q \Delta x^q + \sum_{m=q+1}^p \mu_m \Delta x^m \approx \mu_q \Delta x^q \quad (8)$$

when $p \geq q$, for constants μ_m depending on the truncation error coefficients of the finite difference stencil.

The proof is in App. A.1. Even without numerical error or noise, the learned parameter w has an error depending on the stencil order. Counterintuitively, increasing the polynomial degree of the dataset is counterproductive.

3.3 Training Dynamics for a Linear Model

Suppose now, we wish to learn a matrix \mathbf{W} which converges to the action of a solution operator \mathbf{A} . To determine the expected \mathbf{A} , the Green’s function needs to be discretized relative to the discrete measurement space. The continuous forcing function can be constructed by $f(x) = \sum_i \mathbf{f}_i \psi_i(x)$ where ψ_i is a basis of the grid discretization. The discrete solution operator is thus,

$$\mathbf{u}_i = \sum_j \left[\int_0^1 G(x_i, s) \psi_j(s) ds \right] \mathbf{f}_j \quad (9)$$

with the matrix in brackets defines \mathbf{A} . The MSE loss over the dataset for this model is

$$\mathcal{L} = \frac{1}{N} \sum_{n=1}^N \left\| \mathbf{W} \mathbf{f}^{(n)} - \mathbf{u}^{(n)} \right\|_2^2 \quad (10)$$

More generally, suppose the data is sampled uniformly over subspaces of \mathbb{R}^n such that \mathbf{B} is the matrix of rank $p + 1$ of coefficients satisfying $f(x_i) = \mathbf{f}_i = \mathbf{B} \mathbf{c}$. For example, a polynomial function space can use the Vandermonde matrix $\mathbf{B}_{ij} = [1, x_i, x_i^2 \dots x_i^p]$. By (9), there exists a matrix \mathbf{A} such that all training and test data satisfies $\mathbf{u} = \mathbf{A} \mathbf{f}$. The following result shows that out of distribution generalizations *cannot* be expected:

Theorem 3.2. *Applying gradient descent on training dataset $\{\mathbf{u}^{(n)}, \mathbf{f}^{(n)}\}$ sampled from a function space \mathcal{F}_{train} , the model weights \mathbf{W} will converge to projection of the true operator \mathbf{A} onto the subspace of \mathcal{F}_{train} . Let the forcing functions be sampled by $\mathbf{f}^{(n)} = \mathbf{B} \mathbf{c}^{(n)}$ where each component of \mathbf{c} is sampled independently with $\mathbb{E}[\mathbf{c}_i] = 0$. Optimizing the loss (10) using gradient descent with an initial condition \mathbf{W}^0 will converge to*

$$\mathbf{W}^* = \mathbf{A} \mathbf{U} \mathbf{U}^T + \mathbf{W}^0 (\mathbf{I} - \mathbf{U} \mathbf{U}^T). \quad (11)$$

where \mathbf{U} is the left orthogonal basis of \mathbf{B} of shape $N_{grid} \times (p + 1)$.

The proof is in App. A.3. The learned matrix will converge to the projection of the true operator \mathbf{A} onto the subspace of data F , $\mathbf{A} \mathbf{U} \mathbf{U}^T$, plus an initial error/noise that is orthogonal to the subspace of the data. This result is irrespective of the amount of data and the discretization, and as such, is actually a quite pessimistic result. In particular, \mathbf{A} is only learned iff the dimension of subspace of \mathbf{f} is of equal rank with \mathbf{A} . The finer the discretization, the greater the “quality” of the data needed (e.g. dimension of the subspace).

4 Experiments

We examine eight different types of ML models in different settings: parameter fitting inverse problems where the DE is known (finite difference, PINN), black-box models (linear, deep linear, multilayer perceptron), SciML black-box models (DeepONet, Neural Operator), and physics informed learning models (Physics Informed Deep ONet). The theoretical closed form error estimates are replicated empirically. We then demonstrate that generalization can be inferred from data with careful cross-validation. The results are replicated in the presence of noise and on different linear PDEs. Finally, we demonstrate that the Green’s function operator can be extracted from black-box models. App. B details software, hardware, and hyperparameters. App. D contains additional results on grid size variation.

A total of 25 different datasets are constructed using the function spaces described in Section 3.1: one piecewise linear dataset (FEM) and $p \in [1, 8]$ for polynomial, sine, and cosine spaces. For each choice ($type, p, N_{grid}$), we generate 10,000 examples to represent the infinite data limit. Each dataset is normalized to have unit norm in u to (1) minimize the effects of numerical ill-conditioning and round-off errors in the $p \geq 5$ datasets with extreme magnitudes, and (2) make the MSE comparable across datasets.

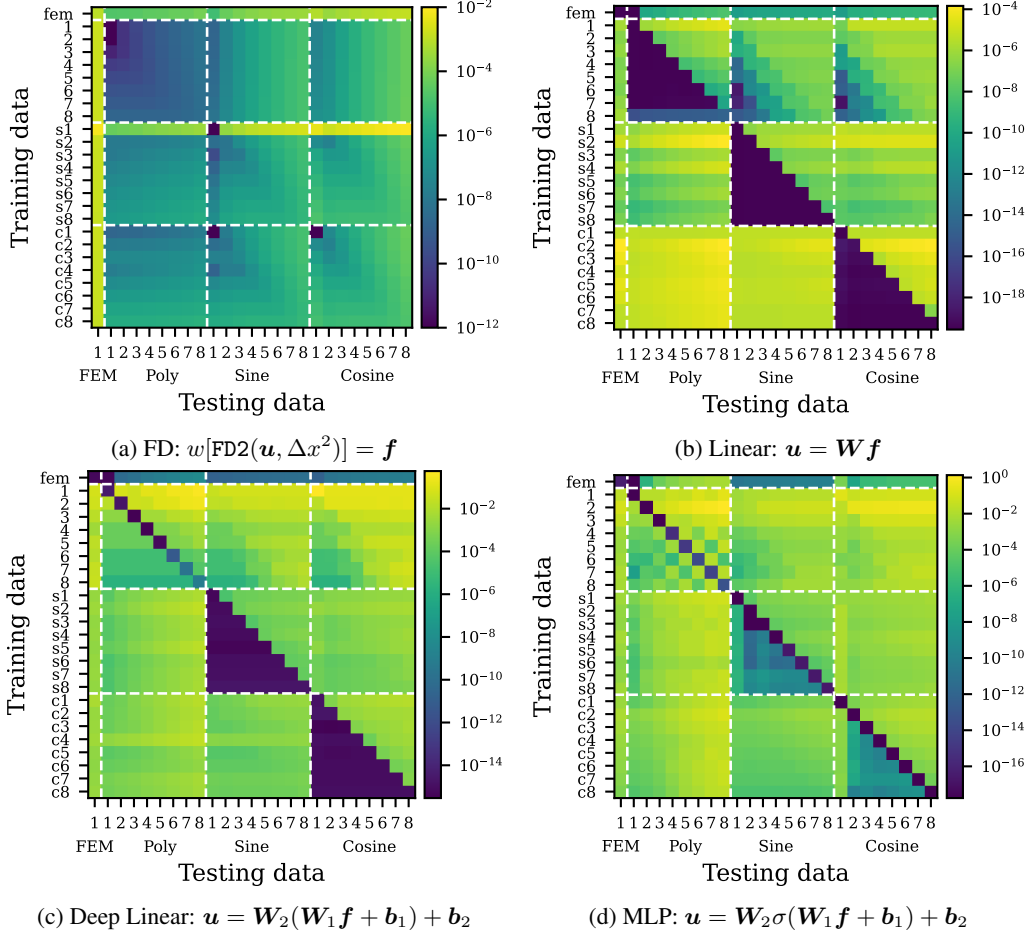


Figure 4: Cross-evaluation error heatmaps for four model types. Rows: training set; columns: test set. Dashed lines separate function class families; cells left of each cell are subspaces. Color shows log-scale MSE (sharp transitions $\approx \times 10^{10}$). The blue lower triangular blocks in 4b and 4c indicate generalization with $\mathcal{L}(w, \mathcal{F}_{test}) \lesssim \mathcal{L}(w, \mathcal{F}_{train})$ when $\mathcal{F}_{test} \subseteq \mathcal{F}_{train}$.

4.1 Comparison of Empirical Errors to Analytical Theory

The theoretical results can be used to compute predicted optimal parameters, allowing for a priori estimations of errors as shown in Fig. 2. The result in Theorem 3.1 can analytically solve expressions of w as in App. A.2. The result Theorem 3.2 can analytically predict $\mathbf{W}(p)$ using the procedure in App. A.4. The observed qualitative behavior matches that predicted by the theorems.

4.2 PINN Inverse Problem for Parameter Learning

We analyze inverse problem solving using PINNs using the DeepXDE library to learn parameter of the 1D Poisson problem, similar to the finite difference model. Vanilla PINNs are not equation discovery methods but are used as numerical solvers when both the PDE is known and some data points are known. The PDE loss can be naturally coupled unknown parameters in the PINN optimization to solve an inverse problem:

$$\min_{\theta, w} \sum_{x \in grid} \left(w \frac{d^2}{dx^2} N(\theta, x_i) + f(x_i) \right)^2 + (N(\theta, x_i) - u_i)^2 \quad (12)$$

where the neural network parameters θ and the unknown physical constant w (which is expected to converge to the physical constant k) are learned simultaneously. The neural network $N(\theta, x_i) \approx u(x)$

fits to a single solution instance $\{x_i, f_i, u_i\}$. The results in Fig. 3 match that of the finite difference white box method, where the parameter error $w - k$ increases with increasing function space terms.

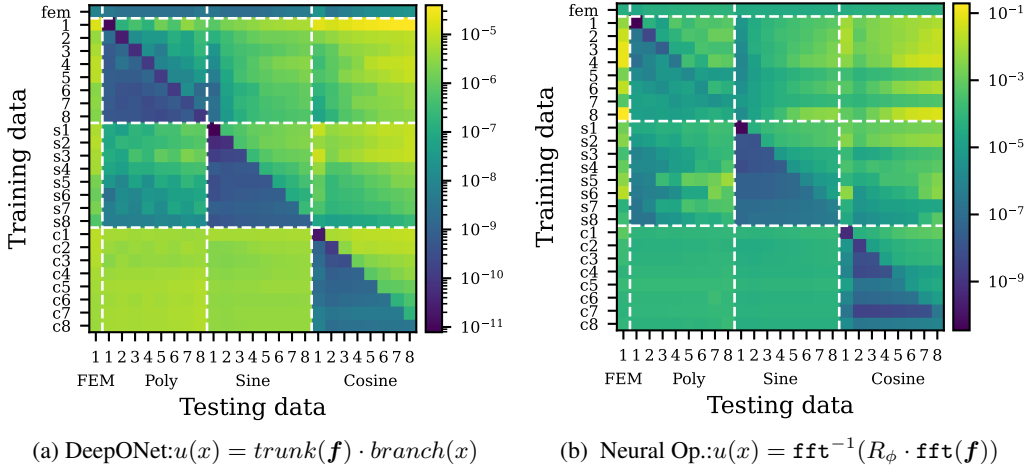


Figure 5: Generalization to out-of-distribution test datasets for the DeepONet and Fourier Neural Operator. The generalization patterns are similar to the Deep Linear models in Fig. 4.

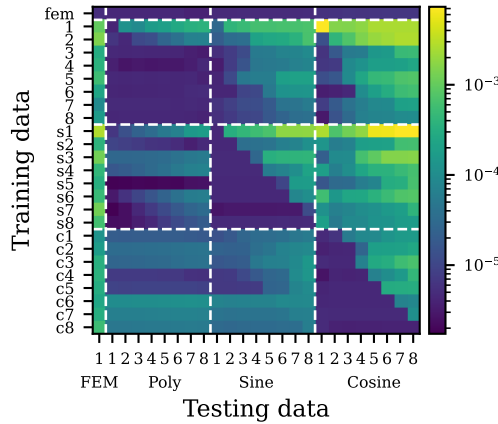


Figure 6: The generalization pattern for the Physics-Informed DeepONet is similar to the Deep ONet in Fig. 5, but with a higher baseline error on the training data.

4.3 OOD Dataset Generalization

We train models from scratch on datasets with $N_{\text{grid}} = 22$ using each of the 25 different datasets. After training, each model is evaluated on the 24 other datasets unseen during training. This results in a 25×25 grid of MSEs for each model, shown in Figs. 4–8 as heatmaps. The model with the best training MSE from 5 runs is chosen to plot the corresponding row in the heatmap. Error bars over multiple seeds are shown in App. C.

Finite Difference Model As predicted by Theorem 3.1, the test error is observed in Fig. 4a increases by both generalizing across higher order functions, moving to the right in the heatmap, and training on higher order functions, moving down in the heatmap. The FEM dataset error is orders of magnitude higher as it violates smoothness requirements for finite differences. See 13 in App. D for further analysis on Δx terms.

Linear Model We turn to Theorem 3.2 to empirically verify its predictions of \mathbf{W} in Fig. 4b. We initialize $W_0 = 0$ and do not use regularization. For each training run, the test error rises sharply when the test data are no longer in a subspace of the training data. There are three clear lower-triangular

blocks in the heatmap representing the three families of nested subspaces, providing evidence for generalization across function subspaces. Increasing polynomial orders decrease the MSE on the cosine and sine datasets (forming pyramid structures in the top middle and right.) The FEM piecewise linear function space along the top row show consistently low MSE in all models.

Deep Linear Models and Shallow Neural Networks We train two basic nonlinear models: a deep linear model and a shallow neural network. As seen in Figs. 4c and 4d, neither models exhibits generalization behavior consistently. The MLP is strongly diagonal, showing that the model will overfit to the training data, and not generalize in any case. The Deep Linear model shows mixed behavior: it exhibits subspace generalization on the sine and cosine datasets but not on the polynomial datasets. As with the linear model, some cross-subspace generalization is observed when the models are trained with piecewise linear functions.

DeepONet and Neural Operators We investigate two models that are designed for learning PDEs: the DeepONet Lu et al. (2021a) and the Fourier Neural Operator Kovachki et al. (2021). The results are displayed in Fig. 5. Both models support flexible x -coordinate distributions; testing in our experiments is still performed on the regular grid for consistency. The DeepONet shows block lower-triangular structure similar to that of the linear model. The diagonals (evaluation on the training distribution) exhibit lower error values, showing a slight overfitting that does not strictly satisfy the subspace generalization. The dips in the trend are clear in Fig. 11e in App. C, where the model could satisfy $\mathcal{L}_{test} \lesssim \mathcal{L}_{train}$ tolerance depending on the application. The Neural Operator has a similar generalization pattern, but did not achieve a low training MSE on all function classes.

Physics-Informed DeepONet We implement a PI-DeepONet following Wang et al. (2021) (Fig. 6), which uses the loss:

$$\min_{\theta} \sum_{f \in \text{data}} \sum_{x \in \text{grid}} \left(-k \frac{d^2}{dx^2} N(\theta, \mathbf{f}, x_i) - f(x_i) \right)^2 + \sum_{x \in \text{boundary}} (\text{BC Loss}(N(\theta, \mathbf{f}, x_i)))^2 \quad (13)$$

where $N(\cdot)$ is the factorized DeepONet that takes the observation point x_i and the forcing function values \mathbf{f} as inputs. Boundary conditions are enforced through an additional loss term. The baseline error is larger than the other models, achieving only 10^{-6} error. The subspace generalization pattern is still evident, although less pronounced due to the raised floor of the error, showing that physics informed losses do not mitigate the subspace limitation.

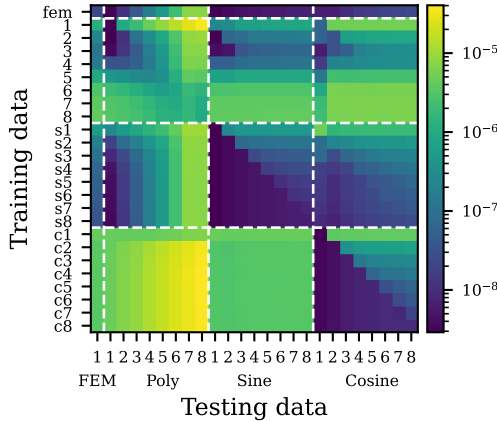


Figure 7: Poisson equation with training data corrupted by noise.

Effect of Noise We investigate the effect of measurement noise on the generalization boundaries by adding normally distributed noise to the 1D Poisson equation training data of u and f . The results are displayed in Fig. 7. Rather than “smearing” the sharp generalization boundaries, noise raises the floor of achievable losses, achieving a lowest error of $\approx 10^{-9}$ compared to 10^{-20} error, and the generalization pattern is still present.

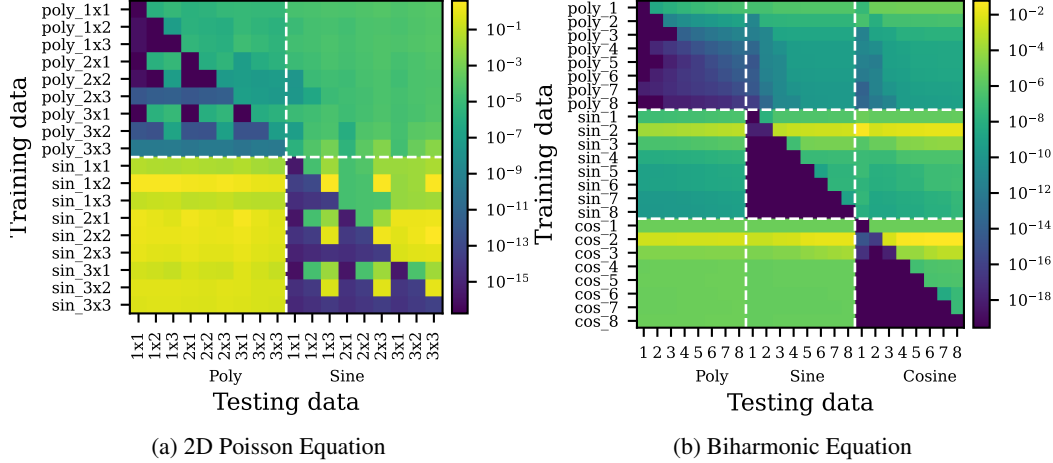


Figure 8: Generalization to out-of-distribution test datasets constructed for the 2D Poisson and Biharmonic equations learned with a linear model.

2D Poisson and Biharmonic Equations We repeat the same experiments for the 1D biharmonic and 2D Poisson equations using a linear model, shown in Fig. 8. The biharmonic equation, $-k \frac{d^4 u}{dx^4} = f$, displays the same block lower-triangular structure as the 1D case. Solutions for the biharmonic are constructed the same way as the 1D Poisson equation. For the 2D Poisson equation, forcing functions are constructed using independent basis functions in x and y , $f(x, y) = \sum_{i=1}^p c_i \sin(\pi i x) \sum_{j=1}^q d_j \sin(\pi j y)$. This exhibits subspace generalization independently in each spatial direction, producing the Sierpiński-triangle-esque pattern. This shows that the results hold generally for linear PDEs, as implied by Theorem 3.2.

4.4 Extracting Green’s functions from black-box models

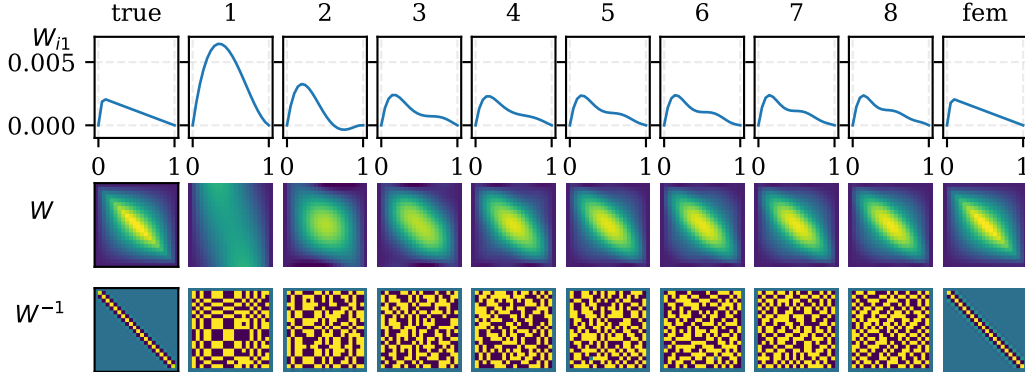


Figure 9: Visualization of the parameter matrix \mathbf{W} of the linear model as the dataset order increases. The top row displays one row W_{i1} of the matrix, the row vector corresponding to the impulse at point $x = \Delta x$. It can be seen to converge to the shape of a Green’s function. The middle row shows the entire matrix as a heatmap, and the bottom displays its inverse. The learned matrix converges incrementally towards the expected matrix (visualized from left to right) as terms are incrementally added to the training dataset. When the model is trained on the FEM dataset, it is possible to invert the learned \mathbf{W} and yield a banded structure of a local stencil. Parameters learned on all other dataset types cannot be inverted reliably.

The Green’s function is defined as the impulse response of the solution operator. Given a trained model, the action of the Green’s function can be approximated by applying a test function $\hat{f}_k = \delta_{kj} = e_j$

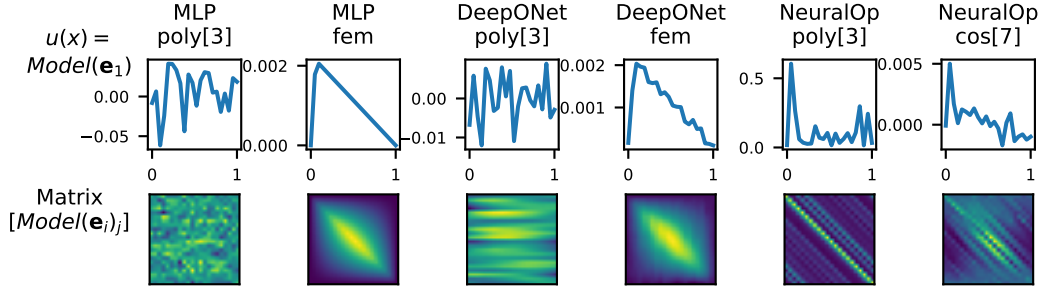


Figure 10: Visualization of test function evaluations, $\text{Model}(e_i)$, on black-box models can reveal Green’s function structure (bottom row). The top row shows one test function evaluation at the node $x = \Delta x$, and the bottom row shows a matrix constructed from model evaluations for all test functions. The colormap scale matches the y-scale of the corresponding plot above them.

(the one-hot vector at index j) to extract the structure using the relation

$$\mathbf{A}_{ij} \leftrightarrow \text{Model}(\mathbf{f} = \mathbf{e}_j)_i. \quad (14)$$

For the linear model, this is the same as inspecting the weight matrix, $\mathbf{A}_{ij} \leftrightarrow \mathbf{W}_{ij}$. Fig. 9 elaborates on Fig. 1 to show the convergence of the weight matrix to the derived analytical solution for increasing modes (or complexity) of data. For lower orders p , the extracted functions are inscrutable, even though the model achieves low error on the training set. Training the linear model on the FEM dataset is sufficient to recover an accurate Green’s operator \mathbf{A} . It is even possible to invert the weight matrix ($\mathbf{W}^{-1} = \hat{\mathbf{L}}$) to uncover a local stencil structure, which is evident in its tridiagonal appearance.

Fig. 10 shows that it is also possible to extract the Green’s functions for deep models by evaluating the nonlinear models on one-hot inputs $\mathbf{f} = \mathbf{e}_j$. For $p = 3$, there is no apparent structure, even though the model achieves low MSE on the training set. The expected structure is extracted using the MLP and DeepONet when they are trained on FEM data. The structure is somewhat evident for the Fourier Neural Operator with the $\text{cos}[7]$ training run, but no others.

5 Conclusion

Learning spatially dependent problems is limited by the underlying function space of the training data and the observation discretization. We theoretically proved that this barrier exists on the simplest problem — the Poisson problem — on parameter fitting finite differences and linear models. We illustrated that carefully choosing the training data can mitigate this issue and that it is possible to generalize to other function spaces, which can inform data collection and cross-validation techniques. As another form of validation, black-box models can be directly interpreted as integrated Green’s functions when they generalize effectively across many test domains. However, this is still pessimistic and presents a headwind for discovering unknown physics from real world data, given the inherent limitations in real world data collection. Confoundingly, different types of ML models can exhibit different and sometimes opposing generalization behaviors.

We demonstrated this behavior across a wide range of representative model types, from simple parameter fits to models designed for PDE learning. Physics informed losses which incorporate prior knowledge (e.g., PINNs and Physics Informed DeepONets) suffer the same subspace limitation as pure black-box models. Our analysis suggests that even the strongest physical priors may not mitigate the impact of the training data distribution.

While our theory required a priori knowledge of how the dataset was constructed, our results suggest that extracting generalized scientific knowledge may require new methods capable of compensating for these limitations by discovering the underlying subspace of the data. We propose this methodology to be an evaluation benchmark on future development of learning physics. As we have seen that even linear DEs can pose a challenge, we recommend that future proposals for DE learning techniques measure cross-set generalization.

Impact Statement

This paper analyzes limitations in discovering underlying physics from data across an entire spectrum of modeling approaches, with implications for evaluation and validation in scientific ML. These findings are relevant for applications in physics and engineering, where understanding out-of-distribution behavior is important for safe real-world deployment. The work does not introduce new capabilities with direct societal risk.

Acknowledgments

Placeholder for blind review.

References

- Baratta, I. A., Dean, J. P., Dokken, J. S., Habera, M., Hale, J. S., Richardson, C. N., Rognes, M. E., Scroggs, M. W., Sime, N., and Wells, G. N. Dolfinx: The next generation fenics problem solving environment, December 2023. URL <https://doi.org/10.5281/zenodo.10447666>.
- Boullé, N., Earls, C. J., and Townsend, A. Data-driven discovery of green’s functions with human-understandable deep learning. *Scientific reports*, 12(1):4824, 2022.
- Boullé, N., Halikias, D., and Townsend, A. Elliptic pde learning is provably data-efficient. *Proceedings of the National Academy of Sciences*, 120(39):e2303904120, 2023.
- Cao, S. Choose a transformer: Fourier or galerkin. *Advances in neural information processing systems*, 34:24924–24940, 2021.
- Gin, C. R., Shea, D. E., Brunton, S. L., and Kutz, J. N. Deepgreen: deep learning of green’s functions for nonlinear boundary value problems. *Scientific reports*, 11(1):21614, 2021.
- Hansen, D., Maddix, D. C., Alizadeh, S., Gupta, G., and Mahoney, M. W. Learning physical models that can respect conservation laws. In Krause, A., Brunskill, E., Cho, K., Engelhardt, B., Sabato, S., and Scarlett, J. (eds.), *Proceedings of the 40th International Conference on Machine Learning*, volume 202 of *Proceedings of Machine Learning Research*, pp. 12469–12510. PMLR, 23–29 Jul 2023. URL <https://proceedings.mlr.press/v202/hansen23b.html>.
- Kaptanoglu, A. A., de Silva, B. M., Fasel, U., Kaheman, K., Goldschmidt, A. J., Callahan, J., Delahunt, C. B., Nicolaou, Z. G., Champion, K., Loiseau, J.-C., Kutz, J. N., and Brunton, S. L. Pysindy: A comprehensive python package for robust sparse system identification. *Journal of Open Source Software*, 7(69):3994, 2022. doi: 10.21105/joss.03994. URL <https://doi.org/10.21105/joss.03994>.
- Kossaifi, J., Kovachki, N., Li, Z., Pitt, D., Liu-Schiaffini, M., George, R. J., Bonev, B., Azizzadenesheli, K., Berner, J., and Anandkumar, A. A library for learning neural operators, 2024.
- Kovachki, N. B., Li, Z., Liu, B., Azizzadenesheli, K., Bhattacharya, K., Stuart, A. M., and Anandkumar, A. Neural operator: Learning maps between function spaces. *CoRR*, abs/2108.08481, 2021.
- Krishnapriyan, A., Gholami, A., Zhe, S., Kirby, R., and Mahoney, M. W. Characterizing possible failure modes in physics-informed neural networks. *Advances in neural information processing systems*, 34:26548–26560, 2021.
- Krishnapriyan, A. S., Queiruga, A. F., Erichson, N. B., and Mahoney, M. W. Learning continuous models for continuous physics. *Communications Physics*, 6(1):319, 2023.
- Lu, L., Jin, P., and Karniadakis, G. E. Deeponet: Learning nonlinear operators for identifying differential equations based on the universal approximation theorem of operators. *arXiv preprint arXiv:1910.03193*, 2019.

- Lu, L., Jin, P., Pang, G., Zhang, Z., and Karniadakis, G. E. Learning nonlinear operators via deepnet based on the universal approximation theorem of operators. *Nature machine intelligence*, 3(3): 218–229, 2021a.
- Lu, L., Meng, X., Mao, Z., and Karniadakis, G. E. DeepXDE: A deep learning library for solving differential equations. *SIAM Review*, 63(1):208–228, 2021b. doi: 10.1137/19M1274067.
- Nanda, N., Chan, L., Lieberum, T., Smith, J., and Steinhardt, J. Progress measures for grokking via mechanistic interpretability. In *The Eleventh International Conference on Learning Representations*, 2023. URL <https://openreview.net/forum?id=9XFSbDPmdW>.
- Nguyen, T., Pham, M., Nguyen, T., Nguyen, K., Osher, S., and Ho, N. Fourierformer: Transformer meets generalized fourier integral theorem. *Advances in Neural Information Processing Systems*, 35:29319–29335, 2022.
- Ott, K., Katiyar, P., Hennig, P., and Tiemann, M. Resnet after all: Neural odes and their numerical solution. In *9th International Conference on Learning Representations (ICLR)*, 2021.
- Patel, R. G., Manickam, I., Trask, N. A., Wood, M. A., Lee, M., Tomas, I., and Cyr, E. C. Thermodynamically consistent physics-informed neural networks for hyperbolic systems. *Journal of Computational Physics*, 449:110754, 2022.
- Queiruga, A. F., Erichson, N. B., Taylor, D., and Mahoney, M. W. Continuous-in-depth neural networks. *arXiv preprint arXiv:2008.02389*, 2020.
- Raissi, M., Perdikaris, P., and Karniadakis, G. E. Physics-informed neural networks: A deep learning framework for solving forward and inverse problems involving nonlinear partial differential equations. *Journal of Computational physics*, 378:686–707, 2019.
- Rudy, S. H., Brunton, S. L., Proctor, J. L., and Kutz, J. N. Data-driven discovery of partial differential equations. *Science advances*, 3(4):e1602614, 2017.
- Sakarvadia, M., Hegazy, K., Totounferoush, A., Chard, K., Yang, Y., Foster, I., and Mahoney, M. W. The false promise of zero-shot super-resolution in machine-learned operators. *arXiv preprint arXiv:2510.06646*, 2025.
- Sander, M., Ablin, P., and Peyré, G. Do residual neural networks discretize neural ordinary differential equations? In Koyejo, S., Mohamed, S., Agarwal, A., Belgrave, D., Cho, K., and Oh, A. (eds.), *Advances in Neural Information Processing Systems*, volume 35, pp. 36520–36532. Curran Associates, Inc., 2022. URL https://proceedings.neurips.cc/paper_files/paper/2022/file/ecc38927fe5148c66bee64ee8fed1e76-Paper-Conference.pdf.
- Trask, N., Huang, A., and Hu, X. Enforcing exact physics in scientific machine learning: a data-driven exterior calculus on graphs. *Journal of Computational Physics*, 456:110969, 2022.
- Udrescu, S.-M. and Tegmark, M. Ai feynman: A physics-inspired method for symbolic regression. *Science Advances*, 6(16):eaay2631, 2020.
- Wang, S., Wang, H., and Perdikaris, P. Learning the solution operator of parametric partial differential equations with physics-informed deepnets. *Science advances*, 7(40):eabi8605, 2021.
- Yu, Y., Liu, N., Lu, F., Gao, T., Jafarzadeh, S., and Silling, S. Nonlocal attention operator: Materializing hidden knowledge towards interpretable physics discovery. *arXiv preprint arXiv:2408.07307*, 2024.
- Zhu, A., Jin, P., Zhu, B., and Tang, Y. On numerical integration in neural ordinary differential equations. In *International Conference on Machine Learning*, pp. 27527–27547. PMLR, 2022.

A Proofs

A.1 Proof of Theorem 3.1

Proof. The training forcing function and corresponding analytical solution is given by

$$f^{(n)}(x) = -k \sum_{m=0}^p c_m x^m \quad (15)$$

$$u^{(n)}(x) = \sum_{m=-2}^p \frac{c_m x^{m+2}}{(m+2)(m+1)} \quad (16)$$

for coefficients c_m . Recall that a finite difference stencil of accuracy order q will satisfy

$$FD_q(u, \Delta x) = u'' + \mathcal{O}(\Delta x^q). \quad (17)$$

Thus for a polynomial whose true derivative is $\sum c_m x^m$, the finite difference stencil can be written as a polynomial whose coefficients change starting at its accuracy order q ,

$$FD_q(u, \Delta x) = \sum_{m=0}^{q-1} c_m x^m + \sum_{m=q}^p c_m (1 + \zeta_m \Delta x^m) x^m \quad (18)$$

$$:= \sum_m b_m x^m \quad (19)$$

where ζ_m is a bound of the coefficient of error introduced for each term m starting at q by Taylor's theorem. These error terms are dependent upon the finite difference stencil; the following section illustrates two examples. This proof is for the general case. For the usual 3 point stencil, $q = 2$. Simplifying the loss

$$\mathcal{L} = \mathbb{E}_c \left[\int_0^1 \left(w \sum_{m=0}^p b_m x^m - k \sum_{m=0}^p c_m x^m \right)^2 dx \right] \quad (20)$$

$$= \mathbb{E}_c \left[\int_0^1 \left(\sum_{m=0}^p (w b_m - k c_m) x^m \right)^2 dx \right] \quad (21)$$

where $b_m = c_m$ for $m < q$ and $b_m = c_m(1 + \zeta_m \Delta x^m)$ for $m \geq q$. Expanding the square, applying the integral and simplifying using the definition of b_m

$$\mathcal{L} = \mathbb{E}_c \left[\int_0^1 \left(\sum_{j=0}^p \sum_{m=0}^p (w b_m - k c_m)(w b_j - k c_j) x^{m+j} \right) dx \right] \quad (22)$$

$$= \mathbb{E}_c \left[\sum_{j=0}^p \sum_{m=0}^p \frac{(w b_m - k c_m)(w b_j - k c_j)}{m+j+1} \right] \quad (23)$$

$$= \mathbb{E}_c \left[\sum_{j=0}^p \sum_{m=0}^p \frac{(w(1 + \xi_m) - k)(w(1 + \xi_j) - k) c_m c_j}{m+j+1} \right] \quad (24)$$

$$= \sum_{j=0}^p \sum_{m=0}^p \frac{(w(1 + \xi_m) - k)(w(1 + \xi_j) - k) \mathbb{E}_c [c_m c_j]}{m+j+1} \quad (25)$$

where we let $\xi_m := \zeta_m \Delta x^m$. Since c_m are iid, then $\mathbb{E}[c_m c_j] = \mathbb{E}[c_m^2] \delta_{mj}$. This lets us only consider the diagonal terms of the sum,

$$\mathcal{L} = \sum_{m=0}^p (w(1 + \xi_m) - k)^2 \frac{\mathbb{E}_c [c_m^2]}{2m+1}. \quad (26)$$

Taking the derivative with respect to w

$$\frac{d\mathcal{L}}{dw} = \sum_{m=0}^p 2(1 + \xi_m)(w(1 + \xi_m) - k) \frac{\mathbb{E}_c [c_m^2]}{2m + 1}. \quad (27)$$

Setting $d\mathcal{L}/dw = 0$, the minima is at

$$w = \frac{\sum_{m=0}^p (1 + \xi_m) \frac{\mathbb{E}_c [c_m^2]}{2m+1}}{\sum_{m=0}^p (1 + \xi_m)(1 + \xi_m) \frac{\mathbb{E}_c [c_m^2]}{2m+1}} k. \quad (28)$$

By assumption that the expectations on the second moment are identical for each coefficient c_m , we can simplify and then break up the sum,

$$w = \frac{\sum_{m=0}^p (1 + \xi_m) \frac{1}{2m+1}}{\sum_{m=0}^p (1 + \xi_m)(1 + \xi_m) \frac{1}{2m+1}} k \quad (29)$$

$$= \frac{\sum_{m=0}^{q-1} \frac{1}{2m+1} + \sum_{m=q}^p (1 + \zeta_m \Delta x^m) \frac{1}{2m+1}}{\sum_{m=0}^{q-1} \frac{1}{2m+1} + \sum_{m=q}^p (1 + 2\zeta_m \Delta x^m + \zeta_m^2 \Delta x^{2m}) \frac{1}{2m+1}} k \quad (30)$$

Now by algebraically using this to compute the error term, we have

$$\frac{w - k}{k} = \frac{-\sum_{m=q}^p (\zeta_m \Delta x^m + \zeta_m^2 \Delta x^{2m}) \frac{1}{2m+1}}{\sum_{m=0}^{q-1} \frac{1}{2m+1} + \sum_{m=q}^p (1 + 2\zeta_m \Delta x^m + \zeta_m^2 \Delta x^{2m}) \frac{1}{2m+1}}. \quad (31)$$

Note that $w = k$ if $p < q$ as the numerator vanishes. Conversely, when $p > q$, $w \rightarrow k$ as $\Delta x \rightarrow 0$ at a rate of Δx^q by polynomial division. Furthermore, for a fixed Δx , increasing p . Each additional term adding p adds additional terms: at the very least, the term $\xi_m \Delta x^{2m}$ is always positive, so the magnitude of that term will always increase, even if $\zeta_m \Delta x^m$ has favorable canceling out.

There, the dominant terms are the numerator,

$$\frac{w - k}{k} = \sum_{m=q}^p (\mu_m \Delta x^m) \quad (32)$$

where the particular coefficients μ_m are finite constants that can be derived for particular finite difference rules. \square

A.2 Concrete Example of Error for 3 point stencil

For a given stencil, the above procedure can be executed algebraically to produced the graph in Fig. 2 (center, right). Plugging in the finite difference stencil into Equation (7), the inner value of the expression is

$$\frac{w}{\Delta x^2} \left(\left(\sum_{n=0}^{p+2} c_n (x - \Delta x)^n \right) - 2 \left(\sum_{n=0}^{p+2} c_n x^n \right) + \left(\sum_{n=0}^{p+2} c_n (x + \Delta x)^n \right) \right) - k \sum_{n=2}^{p+2} n(n-1) c_n x^{n-2} \quad (33)$$

For $p = 0$ and $p = 1$, the equation collapses to $w = k$. But when we consider $p = 2$ with quadratic f and quartic u , there is not full cancellation:

$$\mathcal{L} = \mathbb{E}_c \left[\int_0^1 \left(2w (c_0 + 3c_1 x + 6c_2 x^2 + c_4 \Delta x^2) - 2k (c_0 + 3c_1 x + 6c_2 x^2) \right)^2 dx \right] \quad (34)$$

Following the procedure in the proof algebraically, we have

$$w = \frac{3k (105\Delta^2 + 223)}{245\Delta^4 + 630\Delta^2 + 669} \quad (35)$$

which leads an error term

$$\frac{w - k}{k} = \frac{\Delta^2 (-245\Delta^2 - 315)}{245\Delta^4 + 630\Delta^2 + 669} \quad (36)$$

which satisfies the general result and was used to plot the graph in Fig. 2 (center). A similar algebraic equation can be derived for the five point stencil to yield the graph in Fig. 2 (right).

A.3 Proof of Theorem 3.2

Proof. By construction of our dataset and ansatz on \mathbf{A} , the n th sample is $\mathbf{f}^{(n)} = \mathbf{B}\mathbf{c}^{(n)}$ and $\mathbf{u}^{(n)} = \mathbf{A}\mathbf{B}\mathbf{c}^{(n)}$, thus the loss is

$$\mathcal{L} = \frac{1}{2N} \sum_{n=1}^N \|\mathbf{A}\mathbf{B}\mathbf{c}^{(n)} - \mathbf{W}\mathbf{B}\mathbf{c}^{(n)}\|^2 \quad (37)$$

where \mathbf{A}, \mathbf{W} are of size $N_{\text{grid}} \times N_{\text{grid}}$, \mathbf{c} is of size p and \mathbf{B} is size $N_{\text{grid}} \times p$.

Clearly $\mathbf{W} = \mathbf{A}$ is a solution, but if \mathbf{B} is lower rank than \mathbf{A} and \mathbf{W} , there is a nullspace in the least squares equation. Gradient descent moves in the direction of the gradient of the loss

$$\frac{\partial \mathcal{L}}{\partial \mathbf{W}} = \frac{1}{N} \sum_{n=1}^N (\mathbf{A} - \mathbf{W})(\mathbf{B}\mathbf{c}^{(n)}(\mathbf{c}^{(n)})^T \mathbf{B}^T). \quad (38)$$

With the assumption of iid \mathbf{c} , then $\mathbb{E}[c_m c_k] = \mathbb{E}[c_m^2] \delta_{mk}$. For any sampling and basis set, we can rescale $\mathbf{B}_{:,m}$ such that $\mathbb{E}[c_m^2] = 1$ to simplify the following. By linearity of expectation, we have that the expected gradient is simply

$$\frac{\partial \mathcal{L}}{\partial \mathbf{W}} = (\mathbf{A} - \mathbf{W})\mathbf{B}\mathbf{B}^T. \quad (39)$$

The minima will satisfy

$$0 = (\mathbf{A} - \mathbf{W})\mathbf{B}\mathbf{B}^T \quad (40)$$

via the dynamics

$$\mathbf{W}_{t+1} = \mathbf{W}_t - \eta(\mathbf{A} - \mathbf{W}_t)\mathbf{B}\mathbf{B}^T. \quad (41)$$

With initial condition \mathbf{W}^0 , we will show that the sequence converges to

$$\mathbf{W}^* = \mathbf{A}\mathbf{U}\mathbf{U}^T + \mathbf{W}^0(\mathbf{I} - \mathbf{U}\mathbf{U}^T) \quad (42)$$

where \mathbf{U} is the left $N_{\text{grid}} \times (p+1)$ eigenvector matrix of the SVD decomposition $\mathbf{B} = \mathbf{U}\mathbf{D}\mathbf{V}^T$. Define the error at each step t as

$$\mathbf{E}_t = \mathbf{W}_t - \mathbf{W}^* \quad (43)$$

The error can be decomposed into two components. \mathbf{E}^{\parallel} which is in the row space of $\mathbf{B}\mathbf{B}^T$ and \mathbf{E}^{\perp} which is in the null space $\text{null}(\mathbf{B}\mathbf{B}^T) = \mathbf{I} - \mathbf{U}\mathbf{U}^T$. The matrix $\mathbf{B}\mathbf{B}^T = \mathbf{U}\mathbf{D}\mathbf{V}\mathbf{V}^T\mathbf{D}\mathbf{U}^T = \mathbf{U}\mathbf{D}^2\mathbf{U}^T$. Since the gradient update is always in the row space of $\mathbf{B}\mathbf{B}^T$ this implies that \mathbf{E}^{\perp} is constant 0 as the following calculation shows

$$\begin{aligned} \mathbf{E}_0^{\perp} &= \mathbf{W}_0^{\perp} - \mathbf{W}^{*\perp} \\ &= \mathbf{W}_0(\mathbf{I} - \mathbf{U}\mathbf{U}^T) - (\mathbf{A}\mathbf{U}\mathbf{U}^T - \mathbf{W}_0(\mathbf{I} - \mathbf{U}\mathbf{U}^T))(\mathbf{I} - \mathbf{U}\mathbf{U}^T) \\ &= \mathbf{W}_0(\mathbf{I} - \mathbf{U}\mathbf{U}^T) - \mathbf{W}_0(\mathbf{I} - \mathbf{U}\mathbf{U}^T) = 0 \end{aligned}$$

where we used $\mathbf{U}\mathbf{U}^T(\mathbf{I} - \mathbf{U}\mathbf{U}^T) = 0$. Thus, only considering the component parallel to $\mathbf{U}\mathbf{U}^T$, we perform the algebra on the updates to the error,

$$\begin{aligned} \mathbf{E}_{t+1}^{\parallel} &= \mathbf{W}_{t+1}^{\parallel} - \mathbf{W}^{*\parallel} = (\mathbf{W}_{t+1} - \mathbf{W}^*)\mathbf{U}\mathbf{U}^T \\ &= (\mathbf{W}_{t+1} - \mathbf{A}\mathbf{U}\mathbf{U}^T - \mathbf{W}_0(\mathbf{I} - \mathbf{U}\mathbf{U}^T))\mathbf{U}\mathbf{U}^T \\ &= \mathbf{W}_{t+1}\mathbf{U}\mathbf{U}^T - \mathbf{A}\mathbf{U}\mathbf{U}^T \\ &= (\mathbf{W}_t + \eta(\mathbf{A} - \mathbf{W}_t)\mathbf{B}\mathbf{B}^T)\mathbf{U}\mathbf{U}^T - \mathbf{A}\mathbf{U}\mathbf{U}^T \\ &= \mathbf{W}_t\mathbf{U}(\mathbf{I} - \eta\mathbf{D}^2)\mathbf{U}^T - \mathbf{A}\mathbf{U}(\mathbf{I} - \eta\mathbf{D}^2)\mathbf{U}^T \end{aligned}$$

Assuming the singular values of \mathbf{B} are identical,

$$\begin{aligned} &= (1 - \eta D^2)(\mathbf{W}_t^{\parallel} - \mathbf{W}^{*\parallel}) \\ &= (1 - \eta D^2)\mathbf{E}_t^{\parallel}. \end{aligned}$$

Thus, for any $\eta < 1/\max(D^2)$, the components parallel to $\mathbf{U}\mathbf{U}^T$ goes to zero $\mathbf{E}_t^{\parallel} = (1 - \eta)^t \mathbf{E}_0^{\parallel} \rightarrow 0$. As both error terms converges to 0, we have shown $\mathbf{W}_t \rightarrow \mathbf{W}^*$ as desired. \square

A.4 Corollary to Theorem 3.2: Error Estimate

If the Green’s function and data basis is known, the analytical solution \mathbf{A} can be computed to give estimate of error, shown in Fig.2. The procedure is as follows: Compute a matrix of basis functions evaluated at each point in the domain,

$$\mathbf{B}_{ij} := [\phi_0(x_i), \phi_1(x_i), \dots, \phi_p(x_i)] \quad x_i = i\Delta x \quad (44)$$

and compute the SVD of the basis matrix:

$$\mathbf{U}, \mathbf{D}, \mathbf{V} := \text{SVD}(\mathbf{B}) \quad (45)$$

Generate the Green’s function matrix by symbolically integrating the Green’s function using a compact basis:

$$\mathbf{A}_{ij} = \int_{\Omega} \psi_i(s)G(s, x_j)dx \quad (46)$$

where ψ_i is a piecewise linear or piecewise constant basis function centered on x_i . Then, the error starting at any initial matrix \mathbf{W}^0 can be directly computed as

$$\|\mathbf{W}^* - \mathbf{A}\|_F \approx \|\mathbf{W}^0 - \mathbf{A}\mathbf{U}\mathbf{U}^T\|_F \quad (47)$$

where the computation for \mathbf{A} is imperfect from the arbitrary choice of discretization basis $\psi(x)$.

B Procedure Details

The ultimate experiments ran in float32 on a Macbook Pro M3 Max GPU using PyTorch. To initially rule out errors from accelerator hardware, drivers, or numerical precision, we replicated the linear models and deep models in many implementations: using Tinygrad, JAX, and PyTorch; on CPU, NVIDIA 4070 GPU, and Apple Silicon GPU hardware; and varied precision in float32 and float64. The behavior was consistent across all hardware and software variations.

Finite difference experiments were performed using pysindy (Kaptanoglu et al., 2022); the non-temporal spatial problem was implemented by setting $x_{\text{dot}}[i] = f_i$. The PINN, DeepONet, and Physics-Informed DeepONet were trained using the DeepXDE library (Lu et al., 2021b). The Neural Operator is trained using the neuralop library (Kossaifi et al., 2024). The piecewise linear datasets were generated using the finite element method using FEniCS (Baratta et al., 2023).

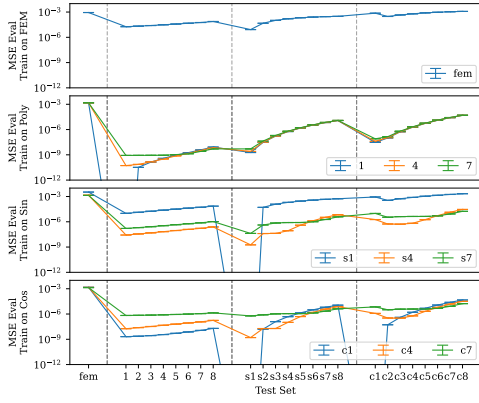
All models were trained using AdamW with weight decay $\lambda = 0.01$. The Linear and Deep Linear models used full-batch training on 10k examples for 2,000 epochs with a linear learning rate schedule from 1e-1 to 1e-6; the Deep Linear has one hidden layer of dimension 100. The MLP (1 layer, hidden dimension 1024, Leaky ReLU) and Fourier Neural Operator (64 modes, hidden dimension 32, GeLU) used batch size 256 for 5,000 epochs with a linear schedule from 1e-2 to 1e-6. The DeepONet used branch tower dimensions [1, 256, 256], trunk tower dimensions [N_{grid} , 256, 256], ReLU activation, batch size 256, and a step schedule from 1e-3 decaying to 1e-6 every 5,000 steps over 20,000 total steps.

C Repeatability of test set generalization

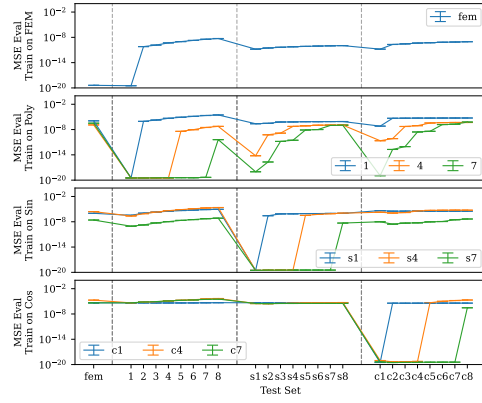
Repeated experiments with different seeds are shown in Figures 11a, 11b, 11c, 11d, 11e, and 11f. Each line on this plot corresponds to training on one function class identified in the legend, which corresponds to a row in the heat map from Figures 4 and 5. The error bars represent min/max over 5 runs, and the line is the average of the five. The repeated runs all show the same qualitative trends of generalization and overfitting in the same regimes for each of the six types of models.

D Grid size generalization

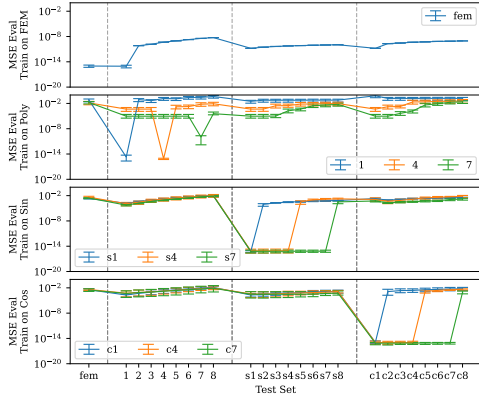
We consider the situation where we train and evaluate models on datasets produced at different grid spacings. Note that Δx is a property of the training data: decreasing Δx in practice would require finer measurements. In Fig. 12, we observe that the shape of the matrix does not change as the grid size increases. The polynomial datasets have the same number of coefficients for each grid size.



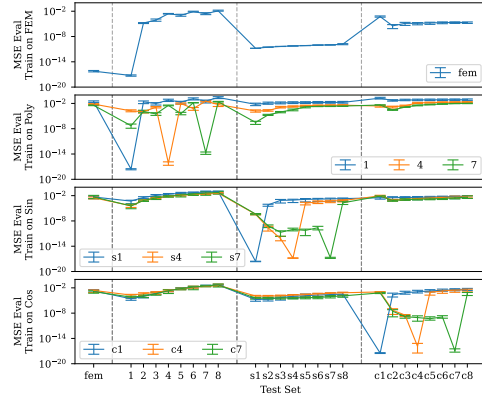
(a) Finite Difference SINDy model.



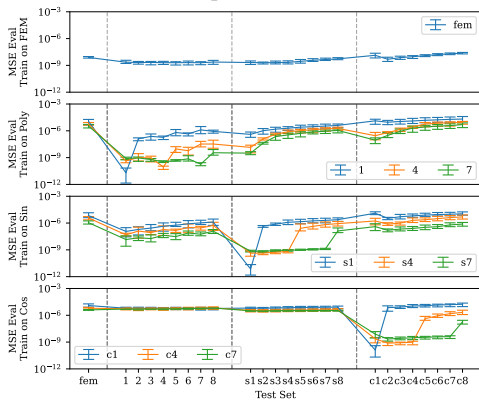
(b) Linear model



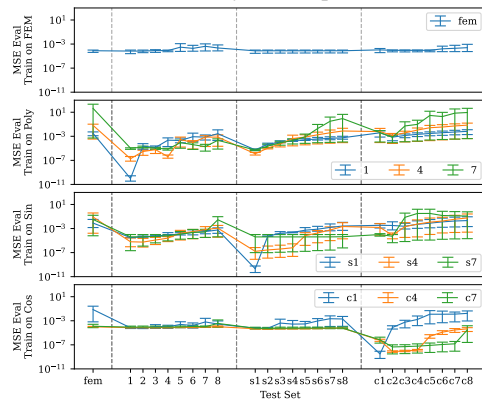
(c) Deep linear model



(d) Multilayer Perceptron



(e) DeepONet



(f) Neural Operator

Figure 11: Generalization errors for all models with five different seeds for each training run. For the Finite Difference SINDy model, the lower y limit is truncated to 10^{-12} ; training on Poly 1, Sine 1 and Cosine 1 achieves error $\approx 10^{-38}$.

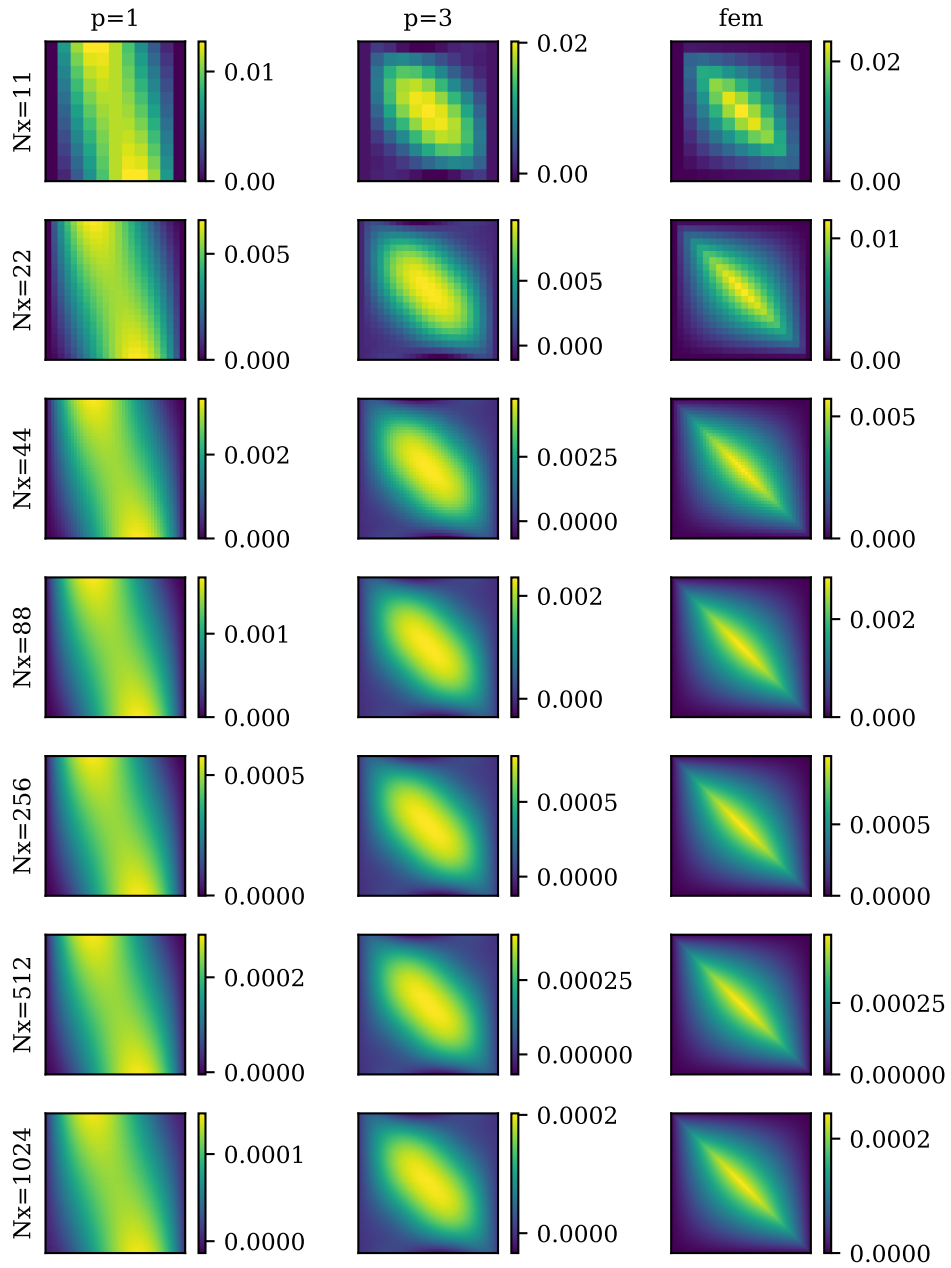


Figure 12: Convergence of the weight matrix W as the grid size increases. The matrix structure is invariant to the discretization, however, each parameter scales proportional to Δx (Eq. 9).

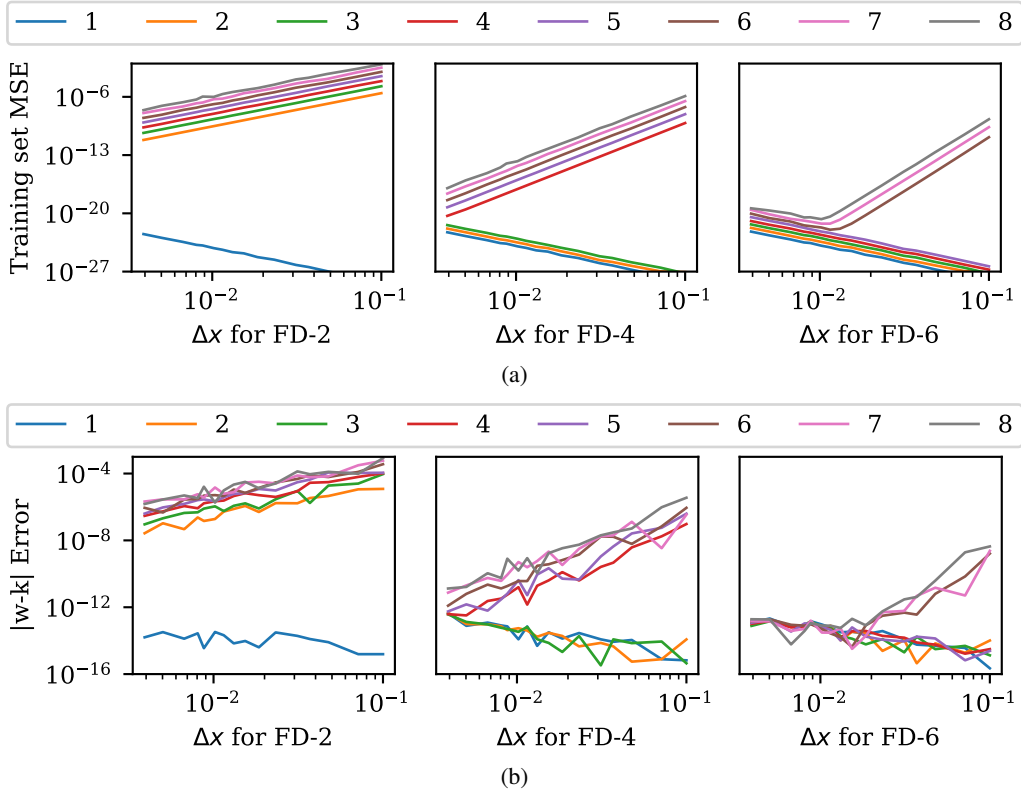


Figure 13: Experiments on SINDy equation discovery as the grid size (x-axis) and training data polynomial function order (line color in legend) is changed. 13a: training data MSE (observable by the scientist). 13b : difference from true parameter (not observable). After convergence, the error tends to increase; we believe this is an artifact of accumulation of floating point error.

However, the rank of “fem” dataset does increase as the piecewise linear functions are sampled the new grid. For the finite difference method in Fig. 13, we do observe a difference in the error. As predicted by Theorem 2, the error on the learned parameter is proportional to both the grid size and polynomial order of the dataset. The order of the stencil does change the rate of convergence towards the true parameter.